Available online at www.sciencedirect.com
ScienceDirect
Comput. Methods Appl. Mech. Engrg. 293 (2015) 1–19
Computer methods in applied mechanics and engineering
www.elsevier.com/locate/cma

# Improved coupling of finite element method with material point method based on a particle-to-surface contact algorithm☆

Z.P. Chen[a], X.M. Qiu[a], X. Zhang[a,*], Y.P. Lian[b]

[a] *School of Aerospace Engineering, Tsinghua University, Beijing, 100084, PR China*
[b] *Department of Mechanical Engineering, Northwestern University, Evanston, IL 60208, USA*

Received 30 January 2015; received in revised form 13 April 2015; accepted 19 April 2015
Available online 25 April 2015

## Highlights

- ICFEMP and IAFEMP methods are developed based on a particle-to-surface contact method.
- The methods allow arbitrary inconsistent meshing between MPM and FEM.
- The efficiency and accuracy of the new methods are much higher than CFEMP and AFEMP.

## Abstract

For extreme deformation problems, material point method (MPM) takes competitive advantages compared with finite element method (FEM) which often encounters mesh distortion. However, for small deformation problems, FEM is still more efficient and accurate than MPM in most cases. Hence, a coupled finite element material point (CFEMP) method and an adaptive finite element material point method (AFEMP) have been proposed by our group to take advantages of both methods. Because the coupling between MPM particles and FEM elements was implemented based on the MPM grid-based contact method, both CFEMP and AFEMP demand a high degree of consistence of meshing between FEM domain and MPM domain. This may lead to over meshing in FEM domain, thus significantly decreases the time step size and increases computational cost as well as data storage. In order to allow arbitrary inconsistent meshing, the CFEMP and AFEMP methods are further improved in this article. The coupling between the MPM particles and FEM elements is implemented based on a particle-to-surface contact algorithm rather than the MPM grid-based contact method, so that the consistent meshing is no more needed. Thus, the meshing of FEM body can be much coarser than the MPM grid. Numerical studies illustrate that the robustness, efficiency and accuracy of the improved CFEMP (ICFEMP) method and the improved AFEMP (IAFEMP) method are much higher than MPM, CFEMP and AFEMP.



*Keywords:* Material point method; Coupled finite element material point method; Adaptive finite element material point method; Impact; Penetration

☆ Supported by the National Natural Science Foundation of China (11390363).
* Corresponding author.
*E-mail address:* xzhang@tsinghua.edu.cn (X. Zhang).

http://dx.doi.org/10.1016/j.cma.2015.04.005
0045-7825/

## 1. Introduction

In recent decades, lots of meshfree and particle methods have been put forward to study challenging mechanical problems, such as penetration, impact, fluid–structure interaction (FSI) and explosion. The material point method (MPM) developed by Sulsky et al. [1,2] is a fully Lagrangian particle method. The material domain is discretized by a set of Lagrangian particles moving through a predefined Eulerian background grid. In each time step, the particles are attached to the background grid and move together with the grid. After solving the momentum equations on the background grid, the solutions are mapped from the grid points to the particles to update their positions and velocities. Finally, the deformed grid is discarded and a new regular grid will be employed in the next time step. Therefore, the mesh distortion caused by extreme deformation is avoided, while numerical difficulties associated with Eulerian method are overcome. MPM has also been used successfully to simulate impact and penetration [2–4], blast [5,6], hyper-velocity impact [7–10], crack propagation [11–13], fragmentation [14–16], multiphase flows [17] and granular flow [18], just to name a few.

Since the particles move in a single-valued continuous velocity field, a no-slip contact constraint is inherent in the standard MPM. York et al. [19] proposed a simple contact algorithm to allow bodies to release. If the bodies are moving away from one another, they move in their own velocity fields to allow separation. Bardenhagen et al. [20,21] developed a contact/friction/separation algorithm in multi-velocity fields. Hu and Chen [22] proposed a contact/sliding/separation procedure in a global multi-mesh environment, but the friction between contact bodies was not considered. However, all these contact methods cannot guarantee the momentum conservation. Huang et al. [3] developed an improved contact method to modify the normal vector on the interface to conserve momentum. To reduce the memory requirement and computational cost, Ma et al. [23] developed a local multi-mesh contact algorithm, in which the multi-mesh is only created at the contacted grid points.

Although MPM can be more accurate, efficient and robust than FEM for problems with severe distortions, it is less accurate and efficient than FEM for problems with small deformation. Besides, MPM requires more computational storage and cost since it saves both grid and particle data. Therefore, it is desirable to couple MPM and FEM to take advantages of both methods.

The coupling of meshfree method and FEM has been studied by researchers in recent years. Attaway et al. [24] coupled SPH with FEM through a master–slave algorithm, in which contact forces is imposed on slave particles and master surfaces to avoid penetration. Similarly, Johnson et al. [25] coupled SPH and FEM to solve high velocity impact problems. After that, Johnson and Stryk [26] extended this coupled particle method by converting damaged or failure elements into particles. Recently, Hu et al. [27] established a coupled FE–SPH model based on a striped-point-in-box searching algorithm for analysis of FSI problems.

Recently, Zhang's group developed four different schemes to couple MPM and FEM [28–32]. In the finite element–material point method [28], the material domain was discretized by a mesh of finite elements, and a computational grid was predefined in the potential large deformation zone. The nodes covered by the grid were treated as MPM particles, and the remaining nodes were treated as FE nodes. In the hybrid finite element–material point method [29], a bar element was introduced into MPM to model reinforced concrete. In the coupled finite element–material point (CFEMP) method [30,31], the FEM body and MPM body were coupled by using the local multi-mesh contact method [23]. In the adaptive finite element material point (AFEMP) method [32], all bodies were initially discretized by finite elements, and the distorted and failed elements were automatically converted into MPM particles during the simulation process. The converted particles were coupled with the remaining FEM nodes by using the local multi-grid contact method [23].

Both the CFEMP and AFEMP methods employ the MPM grid based contact method to couple the MPM particles with FEM nodes. The contact conditions between the MPM domain and FEM domain are only satisfied at the background grid points, but not at the FEM element faces. Furthermore, the grid based contact method also demands a high degree of consistence of meshing between FEM domain and MPM domain. If the meshing of the FEM domain is much coarser than the MPM grid cell, the particles are most likely to penetrate the FEM domain. Consistence of meshing may lead to over meshing of FEM domain, which significantly decreases the time step size and increases computational cost as well as data storage.

In this paper, the CFEMP and AFEMP methods are improved by using a particle-to-surface contact method to satisfy the contact conditions exactly at FEM element faces and to avoid the consistent meshing. The contact forces are calculated based on the Lagrange multiplier method where the MPM particles penetrate FEM element

faces. Moreover, a Coulomb friction model is introduced to allow relative slipping between bodies. The improved methods employ the master element faces rather than the grid points to detect whether the particles penetrate the FEM domain, so that the contact conditions are satisfied exactly between the particles and the FEM element faces. Meanwhile, the consistent meshing is no more needed. Thus, the meshing of FEM body can be much coarser than the grid cells of MPM domain. Moreover, the computational efficiency of the improved methods is much higher than CFEMP and AFEMP since the total number of finite elements is significantly reduced. The improved coupled finite element–material point (ICFEMP) method and the improved adaptive finite element–material point method have been implemented in our 3D explicit MPM code, MPM3D [23,33], and validated by several numerical examples. It shows that ICFEMP and IAFEMP methods are very robust and capable of modelling extreme case whose ratio of element size to grid cell size is far beyond 2.0.

The remaining part of this paper is organized as follows. Section 2 briefly reviews the coupling scheme between FEM and MPM. The detailed formulation of the improved coupled finite element material point method is presented in Section 3. The improve adaptive finite element material point method is also discussed in Section 3. The numerical examples are presented in Section 4 to validate the proposed ICFEMP and IAFEMP. The concluding remarks are summarized in Section 5.

## 2. Coupled finite element material point method

### 2.1. Governing equations

In material domain $\Omega$, the basic equations described in the updated Lagrangian frame are

$$\rho\left(\boldsymbol{X},t\right)J\left(\boldsymbol{X},t\right)=\rho_0\left(\boldsymbol{X}\right) \tag{1}$$

$$\sigma_{ij,j}+f_i=\rho\ddot{u}_i \tag{2}$$

$$\rho\dot{w}^{\text{int}}=D_{ij}\sigma_{ij} \tag{3}$$

with the boundary conditions

$$\begin{aligned}&\left(n_j\sigma_{ij}\right)|_{\Gamma_t}=\bar{t}_i\\&u_i|_{\Gamma_u}=\bar{u}_i\end{aligned} \tag{4}$$

and initial conditions

$$\begin{aligned}&\dot{u}\left(\boldsymbol{X},0\right)=\dot{u}_0\left(\boldsymbol{X}\right)\\&u\left(\boldsymbol{X},0\right)=u_0\left(\boldsymbol{X}\right).\end{aligned} \tag{5}$$

In the above equations, subscripts $i$ and $j$ indicate the components of the spatial variables following Einstein summation convention, subscript 0 denotes the initial value, the comma in the subscripts signifies the covariant differentiation, and the superimposed dot denotes the time derivatives. $\rho$ is the current density, $\boldsymbol{X}$ is the Lagrangian coordinate, $J$ is the Jacobian determinant, $\sigma_{ij}$ is the Cauchy stress, $u_i$ is the displacement, $f_i$ is the body force per unit volume, $w$ is the internal energy per unit volume, $D_{ij}$ is the rate-of-deformation, and $n_j$ is the unit outward normal to the boundary. The displacement boundary and prescribed traction boundary of $\Omega$ are signified by $\Gamma_u$ and $\Gamma_t$, respectively.

Taking the virtual displacement $\delta u_i$ as the test function, the weak form of the momentum equation can be obtained by the weighted residual method as

$$\int_\Omega\rho\ddot{u}_i\delta u_i d\Omega+\int_\Omega\sigma_{ij}u_{i,j}d\Omega-\int_\Omega f_i\delta u_i d\Omega-\int_{\Gamma_t}\bar{t}_i\delta u_i d\Gamma=0 \tag{6}$$

where the displacement boundary conditions must be satisfied as a priori.

### 2.2. MPM solution scheme

In MPM, the material domain is discretized by a set of particles, thus the material density can be approximated by

$$\rho(\boldsymbol{x}) = \sum_{p=1}^{n_p} m_p \delta\left(\boldsymbol{x} - \boldsymbol{x}_p\right) \tag{7}$$

where $m_p$ denotes the mass of particle $p$, $n_p$ signifies the total number of particles and $\boldsymbol{x}_p$ represents the coordinates of particle $p$ and $\delta$ is the Dirac delta function. In each time step, the particles are attached to the background grid. Therefore, the displacement $u_{ip}$ of particle $p$ can be obtained by interpolating the grid nodal displacement $u_{iI}$ as

$$u_{ip} = \sum_{I=1}^{8} N_{Ip} u_{iI} \tag{8}$$

where the subscripts $p$ and $I$ denotes the variables associated with particle $p$ and grid point $I$, respectively,

$$N_{Ip} = \frac{1}{8}(1 + \xi_I \xi_p)(1 + \eta_I \eta_p)(1 + \zeta_I \zeta_p), \quad I = 1, 2, \ldots, 8 \tag{9}$$

is the value of the shape function $N_I(\xi, \eta, \zeta)$ of grid point $I$ evaluated at the site of particle $p$, ($\xi_p \in [1, 1]$, $\eta_p \in [1, 1]$, $\zeta_p \in [1, 1]$) are the nature coordinates of particle $p$, $\xi_I$, $\eta_I$ and $\zeta_I$ take on their nodal value of $(\pm 1, \pm 1, \pm 1)$.

Substituting Eqs. (7) and (8) into Eq. (6) and invoking the arbitrariness of $\delta u_{iI}$ lead to

$$\dot{p}_{iI} = f_{iI} \quad I = 1, 2, \ldots, n_g \tag{10}$$

where

$$m_I = \sum_{p=1}^{n_p} N_{Ip} m_p \tag{11}$$

is the lumped grid nodal mass,

$$p_{iI} = m_I v_{iI} \tag{12}$$

is the grid nodal momentum, $v_{iI}$ is the grid nodal velocity,

$$f_{iI} = f_{iI}^{\text{ext}} + f_{iI}^{\text{int}} \tag{13}$$

is the grid nodal force,

$$f_{iI}^{\text{int}} = -\sum_{p=1}^{n_p} \frac{m_p}{\rho_p} N_{Ip,j} \sigma_{ijp} \tag{14}$$

is the internal grid nodal force,

$$f_{iI}^{\text{ext}} = \sum_{p=1}^{n_p} N_{Ip} \bar{t}_{ip} h^{-1} \frac{m_p}{\rho_p} + \sum_{p=1}^{n_p} m_p N_{Ip} b_{ip} \tag{15}$$

is the external grid nodal force, $\sigma_{ijp} = \sigma_{ij}(\boldsymbol{x}_p)$, $\bar{t}_{ip} = \bar{t}_i(\boldsymbol{x}_p)$, $b_{ip} = b_i(\boldsymbol{x}_p)$ is the body force and $h$ denotes the thickness of the layer of the boundary used to calculate the boundary integral in the last term of the left-hand side of Eq. (6).

### 2.3. FEM solution scheme

The weak form (6) can also be solved by using the finite element method. The displacement $u_i$ at the location of $\boldsymbol{X}$ can be similarly approximated as

$$u_i(\boldsymbol{X}, t) = \sum_{K=1}^{8} N_K\left(\xi(\boldsymbol{X}), \eta(\boldsymbol{X}), \zeta(\boldsymbol{X})\right) u_{iK}(t) \tag{16}$$

where the subscript $K$ indicates the variables of the FE node $K$. Substituting Eq. (16) into Eq. (6) results in

$$\dot{p}_{iK} = f_{iK} \tag{17}$$

where

$$p_{iK} = m_K v_{iK} \tag{18}$$

is the nodal momentum,

$$f_{iK} = f_{iK}^{\text{ext}} + f_{iK}^{\text{int}} \tag{19}$$

is the nodal force,

$$f_{iK}^{\text{int}} = -\sum_e \int_{V_e} N_{I,j}\sigma_{ij} dV \tag{20}$$

is the internal nodal force, and

$$f_{iK}^{\text{ext}} = \sum_e \left( \int_{V_e} \rho N_K b_i dV + \int_{\Gamma_{te}} N_K \bar{t}_i d\Gamma \right) \tag{21}$$

is the external nodal force.

### 2.4. Coupling between finite elements and MPM particles

As a traditional Lagrangian method, FEM is more efficient and accurate than MPM for problems with small deformation. However, in case of extreme deformation, FEM often encounters mesh distortion which leads to numerical difficulties. On the contrary, MPM has the potential to model extreme deformation of materials. Therefore, it is desirable to model the extremely deformed body by MPM and the minor deformed body by FEM, respectively. This section briefly introduces the coupled finite element material point (CFEMP) method [30] in which the MPM body and the FEM body is coupled through the local multi-grid contact method [23].

#### 2.4.1. Contact detection

The contact state can be detected by monitoring velocities of two bodies at the same grid point. If the momenta of two bodies are mapped to the same grid point $I$, the contact may occur. Furthermore, if

$$(v_{iI}^{r,k-1/2} - v_{iI}^{s,k-1/2}) n_{iI}^{r,k} > 0 \tag{22}$$

is satisfied, the FEM body contacts with the MPM body and may penetrate each other in the vicinity of grid point $I$. In Eq. (22), $n_{iI}^{r,k}$ is the unit outward normal of surface of body $r$ at grid point $I$, which can be calculated approximately by the gradient of the mass [21] as

$$n_{iI}^{r,k} = \sum_p N_{Ip,i}^k m_p. \tag{23}$$

Multiplied by $m_I^{s,k} m_I^{r,k}$, Eq. (22) can be rewritten in a momentum form as

$$(m_I^{s,k} p_{iI}^{r,k-1/2} - m_I^{r,k} p_{iI}^{s,k-1/2}) n_{iI}^{r,k} > 0. \tag{24}$$

Using the contact detection condition Eq. (22) or Eq. (24), two bodies may contact earlier than the actual contact time though the space between them is even larger than twice of the grid cell size. In order to prevent the earlier contact, the improved contact detection method proposed by Ma et al. [23] is employed.

*2.4.2. Contact force*

In each time step, the momentum equations of the FEM body $r$ and the MPM body $s$ are first updated independently to obtain the trial solution, assuming they were not in contact. If the FEM body and the MPM body contact at the grid point $I$, a contact force should be imposed between them at the grid point $I$ to prevent penetration. After imposing the contact force $f_{iI}^{b,c,k}$, the momentum $p_{iI}^{b}$ of body $b(b = r, s)$ can be updated by

$$p_{iI}^{b,k+1/2} = \bar{p}_{iI}^{b,k+1/2} + \Delta t^k f_{iI}^{b,c,k} \tag{25}$$

where

$$\bar{p}_{iI}^{b,k+1/2} = p_{iI}^{b,k-1/2} + \Delta t^k f_{iI}^{b,k} \tag{26}$$

is the trial grid nodal momentum, $p_{iI}^{b,k-1/2}$ is the grid nodal momentum of the previous time step, and $f_{iI}^{b,c,k}$ is the contact force applied on body $b$ at time step $t^k$. For stick contact, the updated momentum $p_{iI}^{b,k+1/2}$ must satisfy the velocity continuity condition, namely

$$m_I^{s,k} p_{iI}^{r,k+1/2} - m_I^{r,k} p_{iI}^{s,k+1/2} = 0 \tag{27}$$

The contact force $f_{iI}^{r,c,k}$ for stick contact can be obtained by substituting Eq. (25) into Eq. (27) as

$$f_{iI}^{r,c,k} = -f_{iI}^{s,c,k} = \frac{m_I^{r,k} \bar{p}_{iI}^{s,k+1/2} - m_I^{s,k} \bar{p}_{iI}^{r,k+1/2}}{(m_I^{s,k} + m_I^{r,k})\Delta t^k}. \tag{28}$$

Therefore, the normal and tangential contact forces for stick contact are

$$f_{iI}^{b,\mathrm{nor},k} = f_{jI}^{b,c,k} n_{jI}^{b,k} n_{iI}^{b,k} \tag{29}$$

$$f_{iI}^{b,\tan,k} = f_{iI}^{b,c,k} - f_{iI}^{b,\mathrm{nor},k}. \tag{30}$$

For slip contact, the Coulomb friction model is used to describe the friction at the contact surface, in which the friction force is limited to $\mu \| f_I^{b,\mathrm{nor},k} \|$, where $\mu$ is the friction coefficient. Thus the contact force for slip contact can be calculated by

$$f_{iI}^{b,c,k} = f_{iI}^{b,\mathrm{nor},k} + \min(\mu \| f_{iI}^{b,\mathrm{nor},k} \|, \| f_{iI}^{b,\tan,k} \|) t_{iI}^{b,k} \tag{31}$$

where

$$t_{iI}^{b,k} = \frac{f_{iI}^{b,\tan,k}}{\| f_{iI}^{b,\tan,k} \|} \tag{32}$$

is the unit tangent.

## 3. Improved coupled finite element material point method

In CFEMP, the contact detection is accomplished by monitoring the velocities of two bodies at the same grid point [30]. Therefore, CFEMP requires a high degree of consistence of meshing between FEM body and MPM body, namely

$$\frac{L_{\mathrm{FEM}}}{L_{\mathrm{MPM}}} \approx 1$$

where $L_{\mathrm{FEM}}$ and $L_{\mathrm{MPM}}$ represent the characteristic length of FEM element and MPM grid cell, respectively. If the meshing of the FEM body is coarser than the grid cell, not only the solution accuracy may be seriously deteriorated, but also the MPM particles may penetrate the FEM body. Take the two bodies shown in Fig. 1 as an example, in which the MPM body $s$ is moving towards the FEM body $r$. Because the element size of FEM body $r$ is much larger than the MPM grid cell size, the grid nodal velocities of the cell $i$ are only contributed from the MPM body $s$, but not from the

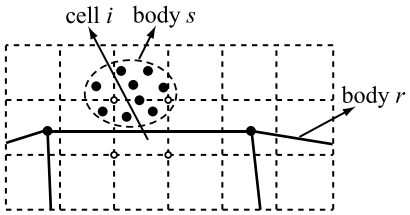


Fig. 1. Illustration of CFEMP with inconsistent meshing.

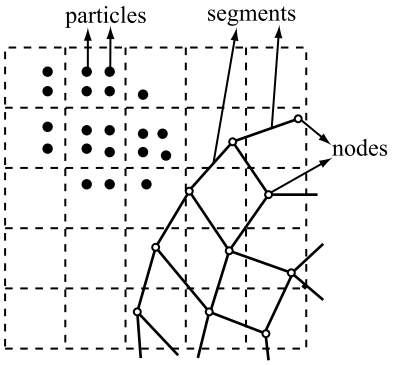


Fig. 2. Bucket-sorting.

FEM body $r$. Based on the contact detection scheme used in CFEMP, the bodies $r$ and $s$ are considered as separated at the grid points of cell $i$, so no contact force will be imposed between them in this case. Therefore, the body $s$ will penetrate the body $r$.

Consistent meshing may lead to over meshing in FEM domain, thus significantly decrease the time step size and increase the computational cost as well as data storage. In order to avoid over meshing in FEM domain, an improved coupled finite element material point (ICFEMP) method is proposed in this section based on a particle-to-surface contact method.

For simplicity, the element faces located on the surface of FEM bodies are termed as segments from now on. In the ICFEMP, we first determine the contact pairs, namely the MPM particles and the corresponding segments where penetration may happen in the global search. Then the exact contact position and the gap between the contact pairs are calculated by using a local search. Finally, a contact force resisting the penetration is imposed between the contact pair if the gap is negative. This step is neglected if the gap is equal to or greater than zero.

### *3.1. Global search*

The global search examines all segments to determine the potential contact particles. The global search costs most of the computer time in the contact algorithm, so a bucket-sorting scheme [34] as shown in Fig. 2 is used to minimize as much as possible the number of computations required. The bucket-sorting scheme uses a cell structure, whose cell sizes are taken to be close to the average element sizes. The key part of this searching procedure is to identify all particles in a cell. The efficiency of global searching could be further improved if we first identify the neighbouring particles of contact boundary so that only the particles near the contact boundary will take part in the bucket sorting.

The cell domain can be described by

$$(x_{\min},\ x_{\max},\ N_x);\quad (y_{\min},\ y_{\max},\ N_y);\quad (z_{\min},\ z_{\max},\ N_z) \tag{33}$$

where $x_{\min}$ and $x_{\max}$ denote the minimal and maximal $x$ coordinates of the cell domain and $N_x$ signifies the number of cells in the $x$ direction. Other variables are analogous to $x_{\min}$, $x_{\max}$ and $N_x$. The cell number in which a particle with coordinates $(x,\ y,\ z)$ is located can be determined by

$$I_p = I_{pz} \times N_x \times N_y + I_{py} \times N_x + I_{px} \tag{34}$$

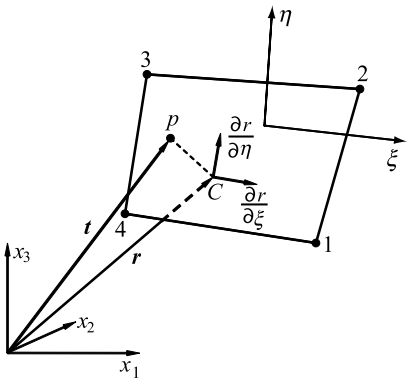


Fig. 3. Local search.

where

$$\begin{aligned} I_{px} &= \text{round}(N_x(x - x_{\min})/(x_{\max} - x_{\min})) \\ I_{py} &= \text{round}(N_y(y - y_{\min})/(y_{\max} - y_{\min})) \\ I_{pz} &= \text{round}(N_z(z - z_{\min})/(z_{\max} - z_{\min})) \end{aligned} \tag{35}$$

where round$(x)$ is a C++ intrinsic function which round down the value of $x$. The MPM particles and segments located in the same cell are labelled as contact pairs.

The size of bucket sorting cell affects the efficiency of global searching, but not the accuracy. Employing a too big cell size will result in too many particles contained in each cell thus increases computational cost, whereas employing a too small cell size will lead to huge amount of cells thus increases data storage. It is suggested that the size of bucket sorting cell should be close to the average element size [34].

In our code, the bucket sorting is performed every time step. However, performing the bucket sorting every several steps should be more efficient. Other researchers have proposed to define an extended 'territory' [35] for each segment and record the cumulative displacement, which was used to judge whether the segment moves out of the territory. In the global searching, they identified all the cells which overlap the territory. The segment and the particle in the same cell were considered to be likely to contact. The bucket sorting was only active for those segments (particles) which run out of their territories in every time step. This algorithm can improve efficiency without affecting its accuracy.

### 3.2. Local search

The contact pairs detected by the global search are likely to contact, but whether contact or not must be further determined. The local search determines the exact contact position and the gap between the contact pairs.

As shown in Fig. 3, a segment can be described by a parametric equation [36,37] as

$$\boldsymbol{r} = f_1(\xi, \eta)\boldsymbol{i} + f_2(\xi, \eta)\boldsymbol{j} + f_3(\xi, \eta)\boldsymbol{j} \tag{36}$$

where $\boldsymbol{i}$,$\boldsymbol{j}$ and $\boldsymbol{k}$ refer to the unit vector in the direction of $x_1$, $x_2$ and $x_3$, respectively, $f_i(\xi, \eta)$ is the global coordinates of the point $(\xi, \eta)$ which can be obtained by interpolating the nodal coordinates of the segment as

$$f_i(\xi, \eta) = \sum_{J=1}^{4} \phi_J(\xi, \eta) x_{iJ} \tag{37}$$

where $\phi_J(\xi, \eta) = \frac{1}{4}(1 + \xi_J\xi)(1 + \eta_J\eta)$ denotes the shape function of the quadrilateral segment, $x_{iJ}$ indicates the $i$th coordinate of the segment's $J$th node.

The local coordinates $(\xi_c, \eta_c)$ of the contact point $C$ on the segment can be determined from

$$\frac{\partial \boldsymbol{r}}{\partial \xi}(\xi_c, \eta_c) \cdot [\boldsymbol{t} - \boldsymbol{r}(\xi_c, \eta_c)] = 0 \tag{38}$$

$$\frac{\partial \boldsymbol{r}}{\partial \eta}(\xi_c, \eta_c) \cdot [\boldsymbol{t} - \boldsymbol{r}(\xi_c, \eta_c)] = 0 \tag{39}$$

where $\boldsymbol{t}$ denotes the position vector of the particle $p$, as shown in Fig. 3.

Eqs. (38) and (39) can be solved by the Newton–Raphson iterative method. Thus, the gap can be calculated by

$$g = \boldsymbol{n} \cdot [\boldsymbol{t} - \boldsymbol{r}(\xi_c, \eta_c)] \tag{40}$$

where

$$\boldsymbol{n} = \frac{\frac{\partial \boldsymbol{r}}{\partial \xi}(\xi_c, \eta_c) \times \frac{\partial \boldsymbol{r}}{\partial \eta}(\xi_c, \eta_c)}{\left| \frac{\partial \boldsymbol{r}}{\partial \xi}(\xi_c, \eta_c) \times \frac{\partial \boldsymbol{r}}{\partial \eta}(\xi_c, \eta_c) \right|} \tag{41}$$

is the unit normal vector pointing outwards at the contact point.

### 3.3. Contact force

If $g \geqslant 0$, the particle do not penetrates the segment, so no further treatment is needed. Otherwise, contact force must be imposed between the particle $p$ and the contact point $C$ to prevent penetration. After imposing the contact force on particle $p$ of body $s$, the updated velocity $v_{ip}^{s,k+1/2}$ is given by

$$v_{ip}^{s,k+1/2} = \bar{v}_{ip}^{s,k+1/2} + \Delta t^k \frac{f_{ip}^{s,c,k}}{m_p^s} \tag{42}$$

where

$$\bar{v}_{ip}^{s,k+1/2} = v_{ip}^{s,k-1/2} + \Delta t^k \sum_{I=1}^{8} N_{Ip} \frac{f_{iI}^{s,k}}{m_I^s} \tag{43}$$

is the trial particle velocity, $v_{ip}^{s,k-1/2}$ is the particle velocity at the beginning of each time step, and $f_{ip}^{s,c,k}$ is the contact force applied on the particle $p$ at time step $t^k$.

Similarly, the updated velocity $v_{ic}^{r,k+1/2}$ of the contact point $C$ on the segment of body $r$ can be evaluated by

$$v_{ic}^{r,k+1/2} = \bar{v}_{ic}^{r,k+1/2} + \Delta t^k \sum_{J=1}^{4} \phi_J(\xi_c, \eta_c) \frac{f_{iJ}^{r,c,k}}{m_J^r} \tag{44}$$

where

$$\bar{v}_{ic}^{r,k+1/2} = \sum_{J=1}^{4} \phi_J(\xi_c, \eta_c)\, \bar{v}_{iJ}^{k+1/2} \tag{45}$$

is the trial velocity of the contact point $C$,

$$f_{iJ}^{r,c,k} = \phi_J(\xi_c, \eta_c) f_{ic}^{r,c,k} \tag{46}$$

and $f_{ic}^{r,c,k}$ is the contact force applied on the contact point $C$.

For stick contact [20,21], the updated velocities of particle $p$ and the contact point $C$ must satisfy the velocity continuity condition

$$(v_{ic}^{r,k+1/2} - v_{ip}^{s,k+1/2}) = 0. \tag{47}$$

By substituting Eqs. (42) and (44) into Eq. (47), the contact force $f_{ic}^{r,c,k}$ for stick contact can be obtained as

$$f_{ic}^{r,c,k} = \frac{m_p^s m_c^r (\bar{v}_{ic}^{s,k+1/2} - \bar{v}_{ip}^{r,k+1/2})}{(m_p^s + m_c^r)\Delta t^k} \tag{48}$$

where $m_c^r$ denotes the equivalent mass of the contact point $C$ defined by

$$\frac{1}{m_c^r} = \sum_{J=1}^{4} \frac{\phi_J^2(\xi_c, \eta_c)}{m_J^r}. \tag{49}$$

Therefore, the normal and tangential contact forces applied on the contact point $C$ are given as

$$f_{ic}^{\mathrm{nor},k} = f_{jc}^{r,c,k} n_{jc}^{r,k} n_{ic}^{r,k} \tag{50}$$

$$f_{ic}^{\tan,k} = f_{ic}^{r,c,k} - f_{ic}^{\mathrm{nor},k} \tag{51}$$

where $n_{ic}^{r,k}$ denotes the unit normal vector pointing out of the segment at the contact point $C$.

For slip contact, the contact force applied at the contact point $C$ can be written as

$$f_{ic}^{r,c,k} = f_{ic}^{\mathrm{nor},k} + \min(\mu \| f_{ic}^{\mathrm{nor},k} \|, \| f_{ic}^{\tan,k} \|) t_{ic}^{r,k} \tag{52}$$

where $t_{ic}^{r,k}$ denotes the unit tangential vector of the segment at the contact point $C$.

Finally, the contact forces applied on the nodes of all segments can be obtained by

$$f_{iJ}^{r,c,k} = \sum_{c=1}^{n_c} \phi_J(\xi_c, \eta_c) f_{ic}^{r,c,k} \tag{53}$$

where $n_c$ is the total number of contact points on all segments, namely, the total number of contact pairs. The contact force applied on the grid points can obtained by

$$f_{iI}^{s,c,k} = \sum_{p=1}^{n_p} N_{Ip} f_{ip}^{s,c,k}. \tag{54}$$

To fully take advantages of both FEM and MPM, Lian et al. [32] developed an adaptive finite element material point (AFEMP) method. All bodies are initially discretized by finite elements, and the distorted and failed elements are automatically converted into MPM particles during the simulation process. The converted MPM particles are coupled with the remaining finite elements through the local multi-grid contact method [23], so AFEMP also requires a high degree of consistence of meshing. Similar to the ICFEMP, an improved adaptive finite element material point (IAFEMP) method can also be developed by replacing the local multi-grid contact method with the particle-to-surface contact method in AFEMP. The IAFEMP method has been implemented in our MPM3D code [23,33], and its detailed formulation will not be repeated here for simplicity.

## 4. Numerical examples

To validate the proposed ICFEMP and IAFEMP methods, several numerical examples, including sphere rolling, perforation of thick plate, water column collapse and free falling of a wedge into water, are investigated in this section.

### *4.1. Sphere rolling*

A series of sphere rolling with different ratios between element size and grid cell size are investigated here to validate the accuracy of the present method. An elastic sphere rolling on an inclined elastic plate at an angle of $\theta$ from the horizontal under gravity, as shown in Fig. 4. The radius of sphere is $r = 1.6$ m, while the size of plate is $20 \times 6.4 \times 1.6$ m. The gravity $g = 10\ \mathrm{m/s^2}$ is vertically downward.

The analytical $x$-coordinate of the sphere's centre can be expressed as

$$x(t) = \begin{cases} x_0 + \dfrac{1}{2} g t^2 (\sin\theta - \mu \cos\theta) & \tan\theta > 3\mu \quad \text{(roll and slip)} \\ x_0 + \dfrac{5}{14} g t^2 \sin\theta & \tan\theta \leqslant 3\mu \quad \text{(roll without slip)} \end{cases} \tag{55}$$

where $x_0 = 0$ is the $x$-coordinate of the initial position of the sphere's centre.

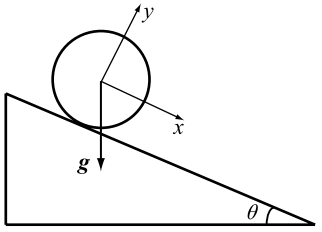


Fig. 4. A sphere rolling on an inclined plate.

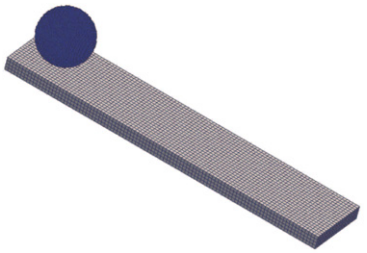

Fig. 5. Typical discretization of a sphere rolling on an inclined plate.

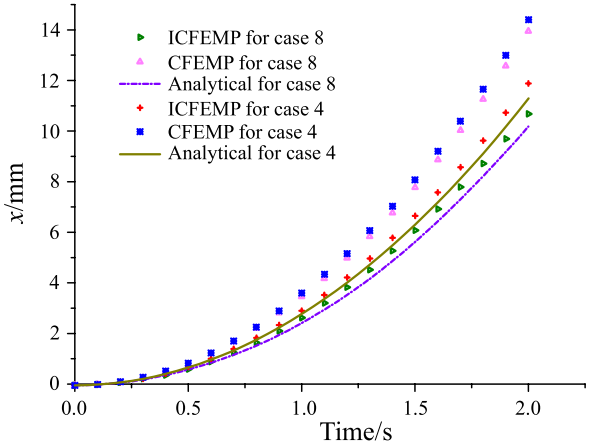


Fig. 6. The time history of the centre-of-mass position for cases 4 and 8 where $R = 8$.

In the simulation, the sphere has a density of $\rho = 1000\ \text{kg/m}^3$, Young modulus of $E = 4.2 \times 10^6$ Pa, and Poisson ratio of $\upsilon = 0.4$. The plate has a density of $\rho = 10,000\ \text{kg/m}^3$, Young modulus of $E = 4.2 \times 10^7$ Pa, and Poisson ratio of $\upsilon = 0.4$. As shown in Fig. 5, the plate is modelled by FEM with fixed boundary condition at the bottom surface, while the sphere is modelled by MPM. The cell size is 0.2 m, and particle space is 0.1 m.

Eight cases are studied. In cases 1–4, the inclined angle $\theta = \pi/4$ with frictional coefficient of $\mu = 0.2$, so that the sphere rolls with slip. The element size of inclined plate is set to 0.2 m, 0.4 m, 0.8 m and 1.6 m, respectively. And accordingly, the ratio $R$ is 1, 2, 4 and 8, respectively. In the last four cases, the inclined angle $\theta = \pi/4$ with frictional coefficient of $\mu = 0.4$, so that the sphere rolls without slip. The element size adopted is the same as that in cases 1–4.

Fig. 6 compares the time history of the centre-of-mass position obtained by ICFEMP with the analytical solutions for cases 4 and 8, in which the element size is 1.6 m. Fig. 6 shows that the numerical results obtained by ICFEMP are in good agreement with analytical solution (55), while those obtained by CFEMP experience significant error when $R \gg 1$.

Table 1 compares the centre-of-mass position at time $t = 2$ s obtained by ICFEMP and CFEMP methods with the analytical solutions for all cases, while Fig. 7 plots the error of the centre-of-mass position with respect to the binary logarithm of $R$. The error of ICFEMP method almost remains constant as the ratio $R$ increases, while that of CFEMP

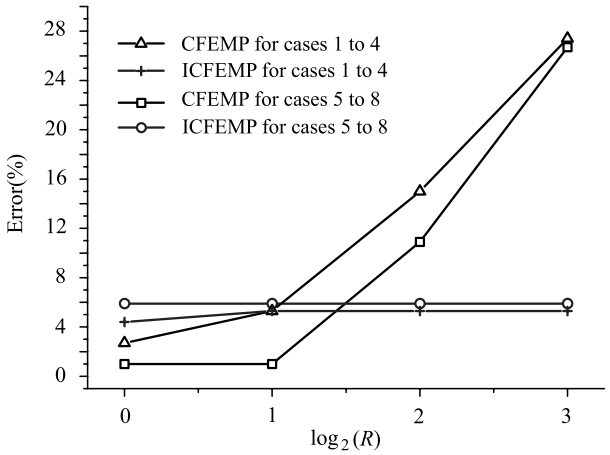


Fig. 7. Error of the centre-of-mass position with respect to $R$ at time $t = 2$ s.

Table 1
The centre-of-mass position at time $t = 2$ s.

| Case | $R$ | Analytical/mm | ICFEMP/mm | CFEMP/mm |
|---|---|---|---|---|
| 1 | 1.0 | 11.2 | 11.8 | 11.6 |
| 2 | 2.0 | – | 11.9 | 11.9 |
| 3 | 4.0 | – | 11.9 | 9.6 |
| 4 | 8.0 | – | 11.9 | 14.4 |
| 5 | 1.0 | 10.1 | 10.7 | 10.2 |
| 6 | 2.0 | – | 10.7 | 10.0 |
| 7 | 4.0 | – | 10.7 | 9.0 |
| 8 | 8.0 | – | 10.7 | 14.0 |

method rapidly increases. The error of CFEMP method rises to about 26% to 28% at $R = 8$. On contrast, the error of ICFEMP is less than 6%. The sphere rolling simulation validates the accuracy of ICFEMP is not sensitive to $R$.

### 4.2. Perforation of thick plate

In order to test the accuracy and computational efficiency of IAFEMP compared to AFEMP, a projectile against oblique thick plate with inclined angle of 30° is investigated. Piekutowski et al. conducted the experiments using ogive-nose hardened steel projectiles and 6061-T651 aluminium plates [38]. The projectile has a length of 88.9 mm and a diameter of 12.9 mm with a 3.0 calibre-radius-head, while the target has a thickness of 26.3 mm and an area of $110 \times 110$ mm.

The projectile and target are discretized with hexahedral elements with unstructured and structured arrangement, respectively. The projectile is modelled as the isotropic hardening plastic material, while the target is modelled as the Johnson-Cook whose yield stress is defined by

$$\sigma_y = (A + B\varepsilon_p^n)(1 + C \ln \dot{\varepsilon}^*)(1 - T^{*m})$$

where $A$, $B$, $C$, $n$ and $m$ are the material constants, $\varepsilon_p$ is the effective plastic strain, $\dot{\varepsilon}^* = \dot{\varepsilon}_p/\dot{\varepsilon}_0$ is the dimensionless plastic strain rate for $\dot{\varepsilon}_0 = 1.0\ \mathrm{s}^{-1}$, and $T^* = (T - T_{\mathrm{room}})/(T_{\mathrm{melt}} - T_{\mathrm{room}}) \in [0, 1]$ is the dimensionless temperature. In addition, the Mie–Gruneisen EOS is applied to update the pressure of target material. In order to overcome the difficulty of mesh distortion, an element is automatically converted into eight MPM particles when its equivalent plastic strain exceeds the given threshold $\varepsilon_c = 0.9$. Besides, the Material failure is under consideration. When the effective plastic strain of a particle reaches the plastic strain $\varepsilon_{\mathrm{fail}} = 1.6$, the particle is assume to be a failed particle, so its deviatoric stress tensor is set to zero. The material constants for the projectile and the target listed in Tables 2 and 3, respectively, are taken from references [38]. The friction between projectile and target is ignored.

Table 2
Material constants of steel projectile.

| $\rho\left(\mathrm{g/mm^3}\right)$ | $E$ (GPa) | $\mu$ | $\sigma_y$ (GPa) | $E_T$ (GPa) |
|---|---|---|---|---|
| 0.00785 | 202 | 0.3 | 1.43 | 14.759 |

Table 3
Material constants of A6061-T651 plate.

| $\rho\left(\mathrm{g/mm^3}\right)$ | $E$ (GPa) | $\mu$ | $A$ (MPa) | $B$ (MPa) | $n$ | $C$ | $m$ |
|---|---|---|---|---|---|---|---|
| 0.0027 | 69 | 0.3 | 262 | 402 | 0.41 | 0.010 | 0.859 |
| $c_0$ (mm/ms) | s | $\Gamma_0$ | $T_{\mathrm{melt}}$ (K) | $T_{\mathrm{room}}$ (K) | | | |
| 5350 | 1.34 | 2.0 | 875 | 293 | | | |

Table 4
Total numbers of elements for projectile and target in each case.

| Case | Target | | Projectile | |
|---|---|---|---|---|
| | Element size (mm) | Number of elements | Element size (mm) | Number of elements |
| 1 | 1 | 314,600 | 2.3 | 12,200 |
| 2 | 1 | 314,600 | 3.8 | 2,268 |
| 3 | 1 | 314,600 | 5.7 | 944 |

Table 5
The projectile's residual velocity and CPU time in different cases.

| Case | $R$ | Residual velocity (m/s) | | | | CPU time (min) | | |
|---|---|---|---|---|---|---|---|---|
| | | Experiment | IAFEMP | AFEMP | MPM | IAFEMP | AFEMP | MPM |
| 1 | 2.3 | 455 | 461 | 430 | 471 | 119 | 184 | 772 |
| 2 | 3.8 | – | 461 | 437 | – | 124 | 141 | |
| 3 | 5.7 | – | 465 | 552 | – | 121 | 112 | |

The experiment with striking velocity of 575 m/s is simulated here. Three different cases with different value of ratio $R$ are investigated to study its effect on the accuracy of both methods, as shown in Table 4. In these cases, the background grid cell size is 1 mm, while the element average size of projectile head is 2.3 mm, 3.8 mm and 5.7 mm, respectively. The total numbers of elements for projectile and target in each case are listed in Table 4.

The residual velocity of the projectile obtained by IAFEMP, AFEMP and MPM are compared with experiment data in Table 5 for different value of ratio $R$. The CPU time consumed by these three methods are also compared in Table 5 to investigate their efficiency. Obviously, the residual velocity obtained by IAFEMP are very close to the experiment data fort any value of $R$, but that obtained by AFEMP method vary greatly as ratio $R$ changes. In this example, the total number of elements in the target keeps the same in all cases, which is about 30 times of that in the projectile, so the differences in computational cost between different cases are mainly due to the differences in contact calculation cost. In all three cases, the total number of contact pairs almost remains the same in IAFEM, so although the cost of AFEMP increases rapidly as the number of elements in the projectile increases, the cost of IAFEMP does not change much.

Table 5 shows that, in order to achieve the same precision, AFEMP must limit the value of ratio $R$ to less than 2 [30]. However the restriction on $R$ is no more needed in IAFEMP. In case 3, although AFEMP costs nearly the same CPU time as IAFEMP, its accuracy is much worse. In case 1, both methods give comparable results, but the cost of IAFEMP is only 65% of AFEMP, 15% of MPM. These studies show that both accuracy and efficiency of IAFEMP are higher than that of AFEMP and MPM. The perforation process obtained by IAFEMP agrees well with the experiment result, as shown in Fig. 8, where Fig. 8(a) shows a sequence of X-ray photographs at three different times and Fig. 8(b) shows the numerical results at almost the same times.

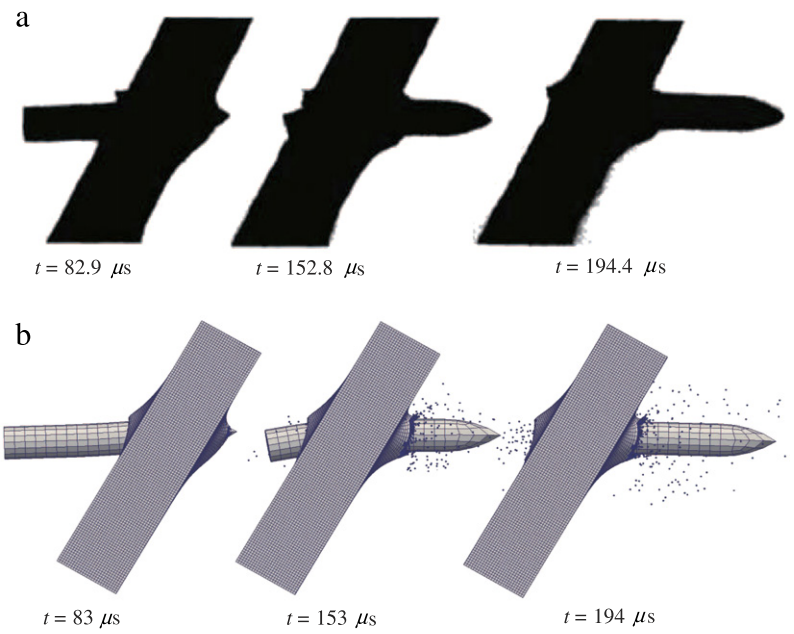


Fig. 8. Perforation process at the striking velocity $v_0 = 575$ m/s: (a) experiment, (b) IAFEMP.

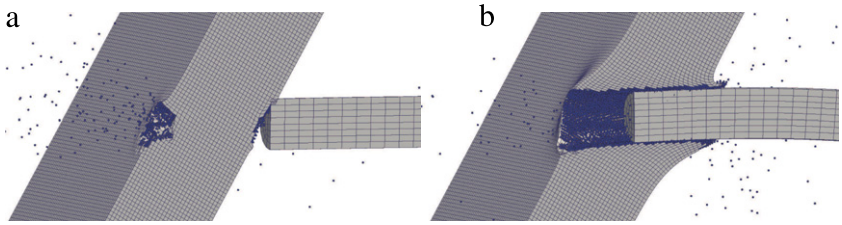


Fig. 9. Sectional view of the simulation results: (a) AFEMP, (b) IAFEMP.

Table 6
The error of residual velocity with respect to time step size.

| d$t$/ms | $1 \times 10^{-5}$ | $2 \times 10^{-5}$ | $3 \times 10^{-5}$ | $4 \times 10^{-5}$ |
|---|---|---|---|---|
| Error/% | 1.8 | 2.2 | 2.5 | 2.9 |

Note that the residual velocity obtained by AFEMP in case 3 is much higher than that measured in experiment. By examining the sectional view of the simulation results as shown in Fig. 9, we can find that in AFEMP simulation result, the projectile penetrates the plate non-physically, as shown in Fig. 9(a).

To study the temporal and spatial convergence of IAFEMP, this problem has been studied with different time step size ($1 \times 10^{-5}$ ms, $2 \times 10^{-5}$ ms, $3 \times 10^{-5}$ ms and $4 \times 10^{-5}$ ms) and different element size of thick plate (1 mm, 2 mm and 4 mm). Tables 6 and 7 list the relative error of residual velocity obtained with different time step size and different element size, which show that the error of residual velocity decrease monotonically as the time step size and element size decrease.

### *4.3. Water column collapse simulation*

The third example is a fluid–structure interaction problem. As shown in Fig. 10, a water column will collapse through a flexible obstacle to the right wall due to the gravity. The water column is $L = 146$ mm wide and $2L$ tall, and the flexible obstacle is $b = 12$ mm wide and 80 mm tall. The distance from obstacle to water column is $L$.

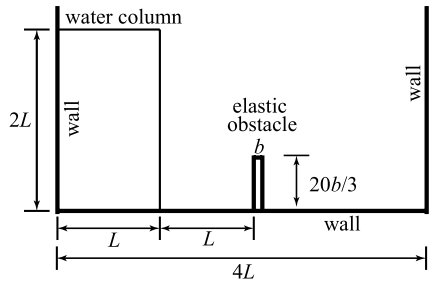


Fig. 10. A water column interacting with an elastic obstacle.

Table 7
The error of residual velocity with respect to element size.

| $h$/mm | 1 | 2 | 4 |
|---|---|---|---|
| Error/% | 2.2 | 11.0 | 19.8 |

The water will collapse freely under the gravity of $g = 9.8$ mm/ms$^2$ downward regardless of the air effect. The flexible obstacle is simulated by FEM with Young modulus $E = 1$ MPa, density $\rho = 2.5$ g/mm$^3$ and Poisson ratio $v = 0$. The water column is simulated by MPM with Mie–Gruneisen EOS ($\rho = 1000$ kg/m$^3$, $c_0 = 1647$ m/s, $s = 1.921$, $\Gamma_0 = 0.1$). In order to keep the surface of water smoothed, the water is assumed to be able to sustain maximum tension of 0.006 MPa. Plane strain is also assumed in the simulation. The sizes of the cell and the element sizes are set to 4 mm, where $R = 1$. The particle space is 2 mm. The whole model consist of 10,608 particles for water, and 60 elements for the obstacle.

Fig. 11 shows that both the deformation of the obstacle and the free surface profile at five different times obtained by ICFEMP agree well with those obtained CFEMP [30] and PFEM [39]. The time history of the deflection at the upper left corner of the obstacle obtained by ICFEMP also agrees well with other available results [30,39,40], as shown in Fig. 12.

### 4.4. Free falling of a wedge into water

It is a great challenging to simulate the free surface and moving solid bodies together. A wedge falling into water is simulated to investigate the capacity of the ICFEMP method for predicting flow phenomena. The velocity variation of the wedge depends on the interaction between the wedge and the surrounding fluid. This problem has been studied by using different methods, such as the level set immersed boundary model [41] and the incompressible SPH method [42]. Zhao et al. also conducted an experiment [43], in which the wedge has a breadth of 500 mm, V-shaped section with a 30° dead-rise angle, as shown in Fig. 13. The total weight is 241 kg. The tank has a width of 2 m and depth of 1 m.

The problem is assumed as plane strain in the simulation. The wedge is modelled as a rigid body, while the water is modelled by the null material with incompressible EOS. The artificial sound speed is chosen as 50 m/s to increase time step size and avoid pressure oscillation [44]. In order to keep the surface of water smoothed, the water is assumed to be able to sustain maximum tension of 0.006 MPa. The acceleration of gravity is taken to be $g = 9.81$ m/s$^2$. The initial velocity of the wedge falling into water is $v_0 = -6.15$ m/s. The sizes of the cell and the average element sizes are set to 20 mm and 28 mm, respectively, while the particle space is 5 mm. The whole model consist of 80,000 particles for water, and 171 elements for the wedge.

Fig. 14 plots the time history of the falling velocity of the wedge obtained by different methods, which shows that the prediction obtained by ICFEMP agrees well with the experiment data before $t = 0.017$ s, but the velocity is over-predicted afterwards. This is possibly due to the approximation of the incompressible model of water and the three-dimensional effects mentioned by Zhao et al. [43].

Finally, in order to examine the effects of the ratio $R$ on the accuracy, the wedge is meshed by 171, 48 and 3 elements, respectively. The value of ratio $R$ in these three cases is 1.6, 3.6 and 14.4, respectively. Fig. 15 compares the water configurations at time $t = 25$ ms obtained by ICFEMP with those obtained by CFEMP with different number of elements in the wedge. The water configurations obtained by ICFEMP fit the wedge shape well no matter how $R$

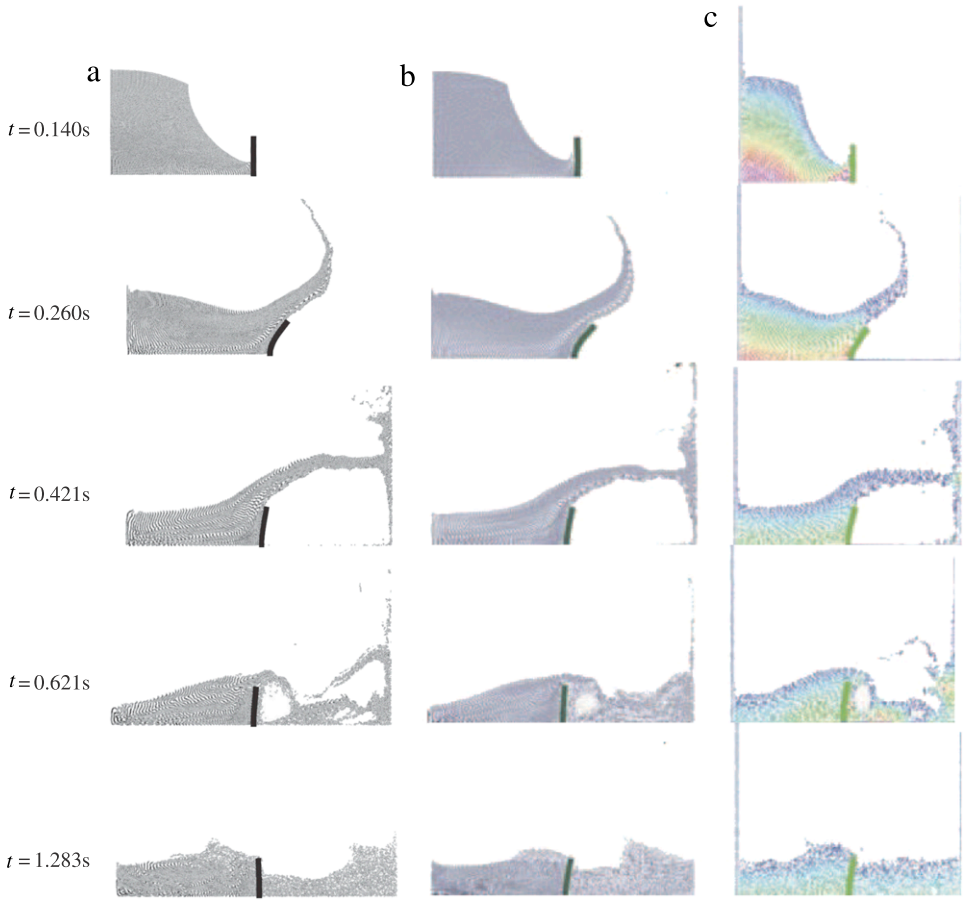


Fig. 11. The deformation of the obstacle and the free surface profile at different times: (a) ICFEMP, (b) CFEMP, (c) PFEM.

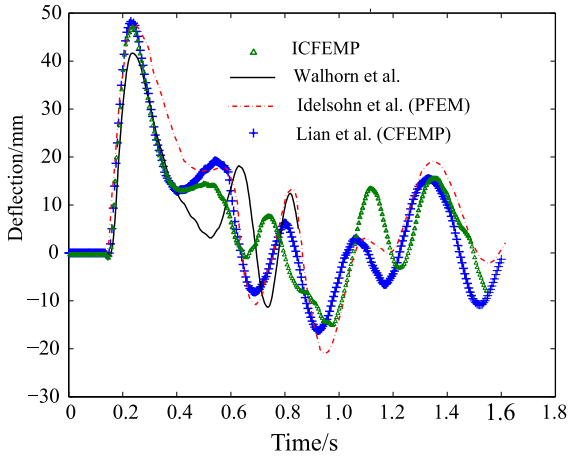


Fig. 12. Comparison of time history of the displacement at the upper left corner of the obstacle between different methods.

varies, but those obtained by CFEMP fit worse and worse as $R$ increases. In the first case, the element size in the lower part of the wedge matches the grid size, so the water does not penetrate the lower part of the wedge in CFEMP results, but penetrates the upper part. In the last two cases, the water penetrates the wedge in CFEMP results everywhere, except at the FEM nodes.

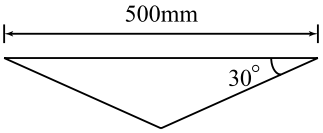


Fig. 13. Wedge section used in the experiment.

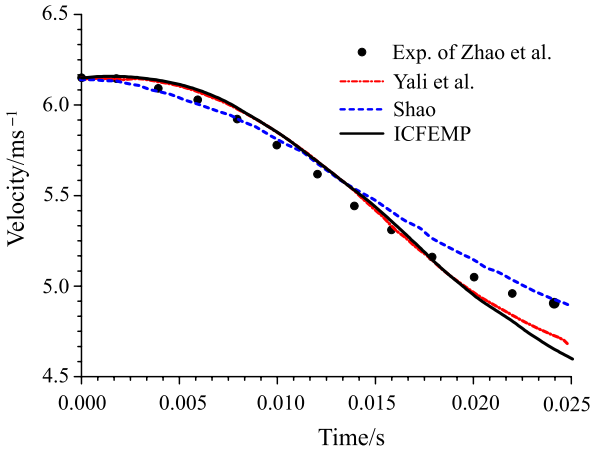


Fig. 14. Time history falling velocity.

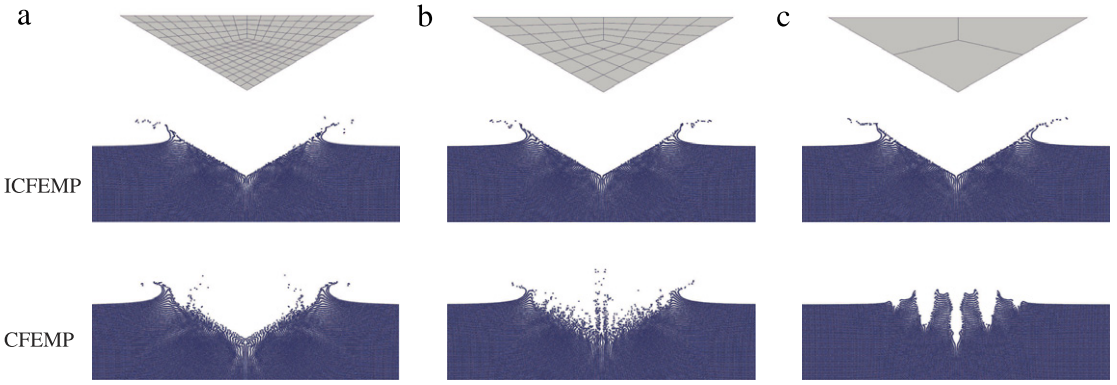


Fig. 15. The water configuration at time $t = 25$ ms obtained with different number of elements in the wedge: (a) 171 elements; (b) 48 elements; (c) 3 elements.

## 5. Conclusion

Because the CFEMP and AFEMP were implemented through the MPM grid based contact method, their accuracy deteriorates rapidly as the ratio of element size to grid cell size increases and over 2.0. Therefore, CFEMP and AFEMP require a high degree of consistence of meshing between FEM domain and MPM domain, thus increases the computational cost and storage requirement significantly. To overcome this limitation, an improved CFEMP and improved AFEMP are proposed based on a particle-to-surface contact algorithm in this paper. A global search is used to identify the potential contact pairs, and then a local search is conducted to further determine the exact contact position and the gap between the particle and the contact point. If the gap is negative, a contact force calculated by the Lagrangian multiplier method is imposed between the contact pair to resist the penetration. Therefore, no particles could penetrate a segment in the improved CFEMP and improved AFEMP methods.

Numerical studies show that the accuracy of ICFEMP and IAFEMP is not sensitive to the ratio of element size to grid cell size. Thus, both the accuracy and efficiency of ICFEMP and IAFEMP are higher than CFEMP and AFEMP. In all numerical examples, the results obtained by ICFEMP and IAFEMP agree well with the analytical solutions or results available in the literature, but the results obtained by CFEMP and AFEMP are only good when the ratio of element size to grid cell size is less than 2.

## References

[1] D. Sulsky, Z. Chen, H.L. Schreyer, A particle method for history-dependent materials, Comput. Methods Appl. Mech. Engrg. 118 (1–2) (1994) 179–196.
[2] D. Sulsky, S.J. Zhou, H.L. Schreyer, Application of a particle-in-cell method to solid mechanics, Comput. Phys. Comm. 87 (1–2) (1995) 236–252.
[3] P. Huang, X. Zhang, S. Ma, X. Huang, Contact algorithms for the material point method in impact and penetration simulation, Internat. J. Numer. Methods Engrg. 85 (2011) 498–517.
[4] W.W. Gong, X. Zhang, X.M. Qiu, Numerical study of dynamic compression process of aluminum foam with material point method, CMES Comput. Model. Eng. Sci. 82 (3) (2011) 195–213.
[5] W.Q. Hu, Z. Chen, Model-based simulation of the synergistic effects of blast and fragmentation on a concrete wall using the MPM, Int. J. Impact Eng. 32 (12) (2006) 2066–2096.
[6] S. Ma, X. Zhang, Y.P. Lian, X. Zhou, Simulation of high explosive explosion using adaptive material point method, CMES Comput. Model. Eng. Sci. 39 (2) (2009) 101–123.
[7] S. Ma, X. Zhang, X.M. Qiu, Comparison study of MPM and SPH in modeling hypervelocity impact problems, Int. J. Impact Eng. 36 (2) (2009) 272–282.
[8] P. Huang, X. Zhang, S. Ma, H.K. Wang, Shared memory OpenMP parallelization of explicit MPM and its application to hypervelocity impact, CMES Comput. Model. Eng. Sci. 38 (2) (2008) 119–147.
[9] W.W. Gong, Y. Liu, X. Zhang, H.L. Ma, Numerical investigation on dynamical response of aluminum foam subject to hypervelocity impact with material point method, CMES Comput. Model. Eng. Sci. 83 (5) (2012) 527–545.
[10] Y. Liu, H.K. Wang, X. Zhang, A multiscale framework for high-velocity impact process with combined material point method and molecular dynamics, Int. J. Mech. Mater. Sci. 9 (2) (2013) 127–139.
[11] J.A. Nairn, Material point method calculations with explicit cracks, CMES Comput. Model. Eng. Sci. 4 (6) (2003) 649–663.
[12] N.P. Daphalapurkar, H. Lu, D. Coker, R. Komanduri, Simulation of dynamic crack growth using the generalized interpolation material point (GIMP) method, Int. J. Fract. 143 (1) (2007) 79–102.
[13] P.F. Yang, Y. Gan, X. Zhang, Z. Chen, W.J. Qi, P. Liu, Improved decohesion modeling with the material point method for simulating crack evolution, Int. J. Fract. 186 (1–2) (2014) 177–184.
[14] B. Banerjee, J.E. Guilkey, T.B. Harman, J.A. Schmidt, P.A. McMurtry, Simulation of impact and fragmentation with the material point method, in: Proceedings of the 11th International Conference on Fracture, Turin, Italy, 2005, p. 689.
[15] L.M. Shen, A rate-dependent Damage/Decohesion model for simulating glass fragmentation under impact using the material point method, CMES Comput. Model. Eng. Sci. 49 (1) (2009) 23–45.
[16] P.F. Yang, Y. Liu, X. Zhang, X. Zhou, Y.L. Zhao, Simulation of fragmentation with material point method based on gurson model and random failure, CMES Comput. Model. Eng. Sci. 85 (3) (2012) 207–237.
[17] D.Z. Zhang, Q. Zou, W.B. VanderHeyden, X. Ma, Material point method applied to multiphase flows, J. Comput. Phys. 227 (6) (2008) 3159–3173.
[18] Z. Wieckowski, The material point method in large strain engineering problems, Comput. Methods Appl. Mech. Engrg. 193 (39-41) (2004) 4417–4438.
[19] A.R. York, D. Sulsky, H.L. Schreyer, The material point method for simulation of thin membranes, International Journal for Numerical Methods in Engineering 44 (1999) 1429–1456.
[20] S.G. Bardenhagen, J.E. Guilkey, K.M. Roessig, J.U. Brackbill, W.M. Witzel, An improved contact algorithm for the material point method and application to stress propagation in granular material, CMES Comput. Model. Eng. Sci. 2 (2001) 509–522.
[21] S.G. Bardenhagen, J.U. Brackbill, D. Sulsky, The material-point method for granular materials, Comput. Methods Appl. Mech. Engrg. 187 (3–4) (2000) 529–541.
[22] W. Hu, Z. Chen, A multi-mesh MPM for simulating the meshing process of spur gears, Comput. Struct. 81 (2003) 1991–2002.
[23] Z. Ma, X. Zhang, P. Huang, An object-oriented MPM framework for simulation of large deformation and contact of numerous grains, CMES Comput. Model. Eng. Sci. 55 (1) (2010) 61–87.
[24] S. Attaway, M. Heinstein, J. Swegle, Coupling of smooth particle hydrodynamics with the finite element method, Nucl. Eng. Des. 150 (1994) 199–205.
[25] G.R. Johnson, Linking of lagrangian particle methods to standard finite element methods for high velocity impact computations, Nucl. Eng. Des. 150 (1994) 265–274.
[26] G.R. Johnson, R.A. Stryk, Conversion of 3D distorted element method for hypervelocity impact simulation, Int. J. Impact Eng. 28 (2003) 947–966.
[27] D. Hu, T. Long, Y. Xiao, X. Han, Y. Gu, Fluid–structure interaction analysis by coupled FE–SPH model based on a novel searching algorithm, Comput. Methods Appl. Mech. Engrg. 276 (2014) 266–286.
[28] X. Zhang, K.Y. Sze, S. Ma, An explicit material point finite element method for hyper-velocity impact, International Journal for Numerical Methods in Engineering 66 (4) (2006) 689–706.

[29] Y.P. Lian, X. Zhang, X. Zhou, Z.T. Ma, A FEMP method and its application in modeling dynamic response of reinforced concrete subjected to impact loading, Comput. Methods Appl. Mech. Engrg. 200 (17–20) (2011) 1659–1670.
[30] Y.P. Lian, X. Zhang, Y. Liu, Coupling of finite element method with material point method by local multi-mesh contact method, Comput. Methods Appl. Mech. Engrg. 200 (2011) 3482–3494.
[31] Y.P. Lian, Y. Liu, X. Zhang, Coupling of membrane element with material point method for fluid-membrane interaction problems, Int. J. Mech. Mater. Sci. 10 (2014) 199–211.
[32] Y.P. Lian, X. Zhang, Y. Liu, An adaptive finite element material point method and its application in extreme deformation problems, Comput. Methods Appl. Mech. Engrg. 241–244 (1) (2012) 275–285.
[33] X. Zhang, Y.P. Lian, Y. Liu, X. Zhou, Material Point Method, Tsinghua University Press, Beijing, 2013.
[34] T. Belytschko, J.I. Lin, A three-dimensional impact-penetration algorithm with erosion, Comput. Struct. 25 (1) (1987) 95–104.
[35] F.J. Wang, J.G. Cheng, Z.H. Yao, A contact searching algorithm for contact-impact problems, Acta Mech. Sin. 16 (4) (2000) 374–382. http://dx.doi.org/10.1007/BF02487690.
[36] D.J. Benson, J.O. Hallquist, A single surface contact algorithm for the post-buckling analysis of shell structures, Comput. Methods Appl. Mech. Engrg. 78 (2) (1990) 141–163.
[37] J. Hallquist, G. Goudreau, D. Benson, Sliding interfaces with contact-impact in large-scale lagrangian computations, Comput. Methods Appl. Mech. Engrg. 51 (1–3) (1985) 107–137.
[38] A.J. Piekutowski, M.J. Forrestal, K.L. Poormon, T.L. Warren, Perforation of aluminum plates with ogive-nose steel rods at normal and oblique impacts, Int. J. Impact Eng. 18 (1996) 877–887.
[39] S.R. Idelsohn, J. Marti, A. Limache, E. Onate, Unified lagrangian formulation for elastic solids and incompressible fluids: Application to fluid–structure interaction problems via the PFEM, Comput. Methods Appl. Mech. Engrg. 197 (2008) 1762–1776.
[40] E. Walhorn, A. Kolke, B. Hubner, D. Dinkler, Fluid–structure coupling within a monolithic model involving free surface flows, Comput. Struct. 83 (25–26) (2005) 2100–2111.
[41] Y. Zhang, Q. Zou, D. Greaves, D. Reeve, A. Hunt-Raby, D. Graham, P. James, X. Lv, A level set immersed boundary method for water entry and exit, Commun. Comput. Phys. 8 (2) (2010) 265–288.
[42] S.D. Shao, Incompressible SPH simulation of water entry of a free-falling object, Internat. J. Numer. Methods Fluids 59 (2009) 91–115.
[43] R. Zhao, O. Faltinsen, J. Aarsnes, Water entry of arbitrary two-dimensional sections with and without flow separation, in: 21st Symposium on Naval Hydrodynamics, 1997.
[44] J.P. Morris, P.J. Fox, Y. Zhu, Modeling low reynolds number incompressible flows using SPH, J. Comput. Phys. 136 (1) (1997) 214–226.